IEEE Transactions on Robotics (T-RO) paper, presented at ICRA 2023, London, UK. Cite as T-RO paper.

Controlling Collision-Induced Aggregations in a Swarm of Micro Bristle-Robots

Zhijian Hao, Siddharth Mayya, Gennaro Notomista, Seth Hutchinson, Magnus Egerstedt, Azadeh Ansari

***Abstract*—Systematically designing local interaction rules to achieve collective behaviors in robot swarms is a challenging endeavor, especially in micro-robots where size restrictions imply severe sensing, communication, and computation limitations. In such robot swarms, performing useful functions is often pre-conditioned on the formation of high-density aggregations which can facilitate collective signaling and information sharing. In this paper, we present a systematic approach to control aggregation behaviors by leveraging the physical interactions in a swarm of 300 3-mm vibration-driven micro bristle-robots that we designed and fabricated. We demonstrate the ability to control the degree of aggregation by varying the motility characteristics of the robots through global vibration frequency and amplitude inputs, after comprehensive characterization, modeling and simulation of the locomotion dynamics and robot interactions. To quantify the degree of aggregation, we also introduce a new metric, the MIPS index (Motility-Induced Phase Separation index), which unlike many existing methods does not require a scenario-specific tuning of parameters. Our investigations reveal how physics-driven interaction mechanisms can be exploited to achieve desired behaviors in minimally equipped robot swarms and highlight the specific ways in which hardware and software developments aid in the achievement of collision-induced aggregations.**

***Index Terms*—Swarms, micro/nano robots, multi-robot systems, aggregation control.**

I. Introduction

ROBOTIC swarms have been demonstrated to be suitable for various tasks including environmental monitoring [1], agriculture [2], construction [3], surveillance [4], and advanced manufacturing [5], [6]. In all these applications, collective behaviors emerge from local interaction rules between the robots in the swarm [7], [8]. A paramount example of collective behavior is *aggregation formation*, defined as the achievement of regions of high robot density. In fact, aggregation plays a fundamental role in the above-mentioned applications as it is a building block upon which more sophisticated behaviors can be synthesized [9]. This is especially relevant in micro- or nano-robot swarms, where aggregation can be leveraged to allow thousands to millions of tiny coordinating robots to perform operations such as targeted drug delivery [10], [11], cell analysis [12] and disease diagnosis [13]. In such scenarios, the formation of aggregates can facilitate critical operations such as information exchange and collective sensing but are complicated to achieve due to the limited motility, sensing, communication, and computational capabilities of micro-robots [14]. Such difficulties can be ameliorated by systematic mechanisms that leverage the physics of interac-

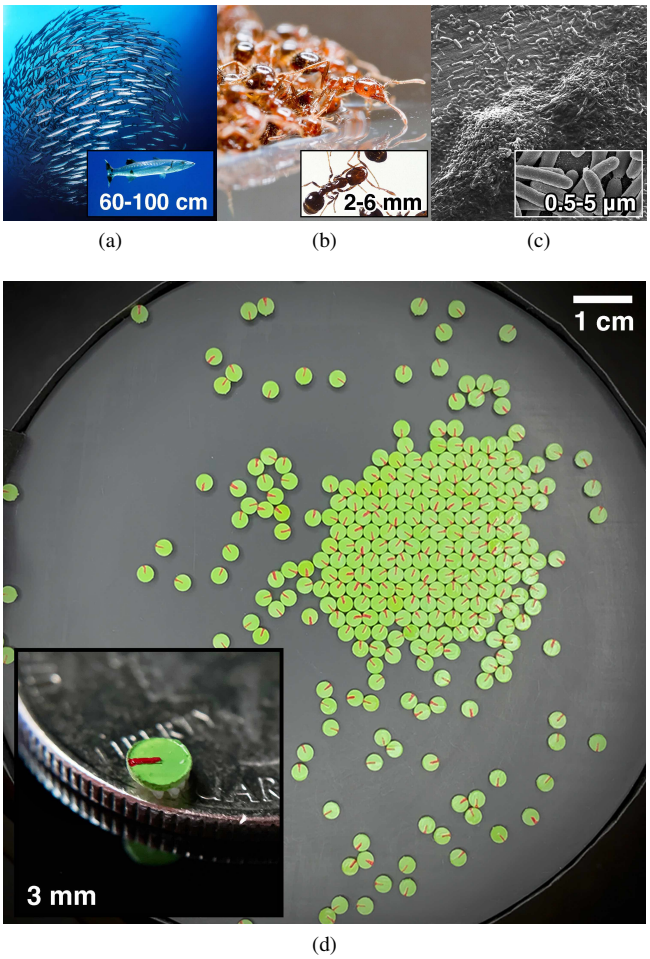

Fig. 1. Naturally occurring collectives and the micro bristle-robot swarm studied in this paper. (a) fish schooling, (b) fire ant raft and (c) biofilm formed by bacteria. (d) Micro bristle-robot swarm in this study can be controlled to present different aggregation behaviors. Inset: 3-mm micro bristle-robot used in this study on the top of a US quarter.[1]

This work is supported by the Institute for Robotics and Intelligent Machines (IRIM) at Georgia Institute of Technology. (*Corresponding author: Azadeh Ansari.*)

Z. Hao and A. Ansari are with the School of Electrical and Computer Engineering at the Georgia Institute of Technology, Atlanta, GA 30332 USA (email: zhao38@gatech.edu; azadeh.ansari@ece.gatech.edu)

S. Mayya is with Amazon Robotics, North Reading, MA, USA (email: mayya.siddharth@gmail.com). This work is not related to Amazon.

G. Notomista is with the Department of Electrical and Computer Engineering, University of Waterloo, Waterloo, ON, Canada (email: gennaro.notomista@uwaterloo.ca).

S. Hutchinson is with Institute for Robotics and Intelligent Machines, College of Computing, Georgia Institute of Technology, Atlanta, GA 30332 USA (email: seth@gatech.edu).

M. Egerstedt is with the Department of Electrical Engineering and Computer Science at the University of California Irvine, Irvine, CA 92697 USA (email: magnus@uci.edu).

IEEE Transactions on Robotics (T-RO) paper, presented at ICRA 2023, London, UK. Cite as T-RO paper.

tions among the robots and with the environment to achieve desired collective behaviors such as aggregation, which we will present in this paper.

Naturally occurring collectives—both living and non-living—demonstrate remarkable collective behaviors across a wide range of spatial and temporal scales [15], [16]. For instance, insect colonies perform sophisticated functions such as traffic regulation [17] and resource collection [18] without any central coordination. Studies on aggregation behavior in these living swarms show how individuals form high-density clusters for functions such as predator avoidance [19], feeding [20], and reproduction [21] (Fig. 1(a) and 1(b)). Micro-organisms such as bacteria and amoebae also demonstrate similar aggregation behaviors precipitated by changes in the motility of individuals in response to local stimuli [22]. For instance, biofilm aggregates in bacterial colonies (Fig. 1(c)) are often induced by fluctuations in the density of bacteria in a given region [23]. Characterizing the interplay between local interaction rules, motility patterns, and environmental factors in these biological systems can facilitate a deeper understanding of the mechanisms behind a large class of systems and serve as further motivation for the work we present in this paper.

Similar observations have been made in inanimate collectives such as artificial nano-swimmers and auto-phoretic colloids, where persistent collisions lead to spontaneous formations of high-density clusters even in the complete absence of an attractive force [24], [25]. This phenomenon is broadly referred to as motility-induced phase separation (MIPS) [26], [27], which is reminiscent of the phase separation well-studied in physical systems at thermodynamic equilibrium [28]. In particular, it has been shown that the density field dynamics of certain active matter systems—defined as systems whose constituent elements consume energy and are thus out-of-equilibrium—can be mapped on an equilibrium system with an analytically computed free-energy density. Research in this emerging area has illuminated exciting ways to apply well-understood ideas from equilibrium statistical mechanics to predict behaviors in systems ranging from fish schools to robot swarms [16], [29]. These investigations provide crucial insights into achieving aggregation behaviors in minimally equipped robot swarms, where limited range interactions necessitate the formation of aggregates for functions like information sharing and quorum-based signaling [9].

In this paper, we study the formation of spontaneous high-density aggregations in a swarm of 300 custom-made micro bristle-robots as shown in Fig. 1(d). The individual robots—endowed with inclined bristles and placed on a vibrating substrate—move in a directed fashion, with their orientation undergoing a diffusive change. As a result of this directed motion, persistent collisions occur among the robots, which are typically resolved when a participating robot changes its orientation. When the density of robots is sufficiently high, this can lead to the formation of robot clusters, resulting in a separation between fast moving individual robots and slow-moving dense robot clusters.

Our previous work [29] demonstrated this clustering effect on a swarm of macro-scale bristle-robots and discussed the conditions under which MIPS-based aggregation can occur. This paper expands on the results in [29] by introducing a novel metric to measure the *degree of aggregation* within a swarm and demonstrating how this metric can be used to facilitate swarm-level control by dynamically changing the motility characteristics of the robots by means of varying vibration inputs. We demonstrate the ability to achieve a range of commanded swarm aggregation levels by switching between a finite set of vibration modes. More specifically, the contributions of this paper can be summarized as follows:

(i) We design and fabricate a swarm of 300 micro bristle-robots with rich vibration-dependent motility characteristics and develop an experimental platform to study the collision-induced aggregation behaviors with extensive characterizations;
(ii) We present a novel metric, the *MIPS index*, to quantify the *extent of aggregation* in the swarm of colliding micro bristle-robots and demonstrate its advantages over existing metrics;
(iii) We highlight how the extent of aggregation in the swarm can be *controlled* by exploiting the physics of their interactions via data-driven characterizations of real experiments.

It is worth noting that the findings presented in this paper are not limited to the micro bristle-robots studied here but may be generalized and adapted to study aggregation in other robot swarms, particularly in millimeter-, micrometer- and even nanometer-scale robot swarms where resource limitations can be overcome by leveraging the physics of interactions of the robots in their environment. For example, in the drug delivery application, acoustic actuation using ultrasound transducers can be used to control in-vivo micro-robots whose motility characteristics are vibration frequency- and/or amplitude-dependent [30], thus achieving controlled aggregations in targeted areas. The paper outlines a framework to model and experimentally characterize such robot systems at both the individual robot and swarm levels, where we design experiments to extract the motion characteristics of individual robots and characterize the influence of inter-robot interactions. In particular, a combination of theoretical modeling and experimentation is used to shed light on how factors such as manufacturing variabilities of the robots, frictional forces experienced during collisions, and edge effects can lead to significant differences between the aggregation characteristics of micro bristle-robot swarms and those of the idealized active matter systems.

The outline of the rest of the paper is as follows: In Section II, we describe the micro bristle-robots considered in this paper along with the vibration platform used for their actuation and control. Section III characterizes the motion of individual micro bristle-robots and demonstrates—via experiments—how

[1]Image copyrights: Swirl of fish barracuda © armiblue, licensed. Sphyraena barracuda in French Polynesia © Hectonichus, CC-BY-SA-4.0. Fire ant raft © Ko and Hu, Georgia Tech, with permission. Fire ants © Stephen Ausmus, public domain. SEM image of a laboratory-grown potable water biofilm © CDC, Janice Haney Carr, public domain. Escherichia Coli © Rocky Mountain Laboratories, NIAID, NIH, public domain.

their motion can be regulated using global vibration inputs. Following this, Section IV uses a data-driven approach to investigate the impact of inter-robot collisions on the motion of individual robots. Section V introduces the MIPS index as a measure of the extent of aggregation in the swarm, and Section VI leverages this metric for open-loop aggregation behavior characterization and closed-loop aggregation control. Section VII concludes the paper.

II. Micro Bristle-Robot and Control Platform

Results from the active matter systems literature illustrate how certain motility characteristics of individuals in a collective, combined with the right interaction mechanisms, can lead to the formation of high-density clusters [26]. However, in order to dynamically adjust the degree of aggregation, we need a swarm of robots that shows wide-ranging and controllable characteristics—preferably via global signals. A vibration-driven bristle-robot is thus a good candidate, due to the simplicity of its locomotion and rich motion dynamics hitherto reported [31]–[37]. Such robots can be actuated via either on-board actuators or a vibrating substrate underneath, and their speed is dependent on both the vibration amplitude and frequency [33], [34]. In addition, recent works show that such micro bristle-robots are ideal candidates for miniaturization and scalable production, thanks to their monolithic design [32]–[34].

The micro bristle-robot used in this study has an overall size of 3 mm $\times$ 3 mm $\times$ 1.5 mm (Fig. 2(a)), which consists of a top body and a set of micron-scale bristles. The bristles have a diameter of 400 μm and are tilted by 60° relative to the horizontal plane. The robots are 3D printed (see Appendix A) and colored for tracking and data collection purposes required for characterizing their dynamics. The fabrication process is illustrated in Fig. 2(b).

When the robot is placed on a vibrating substrate, it consistently gains momentum through collision with the substrate surface, resulting in hopping locomotion. During each collision, the bristle tips are subjected to asymmetrical forces due to their tilt. As a result, the robots gain net lateral locomotion in the direction defined by the bristles' tilt direction. This process is captured via a high-speed camera[2]. Snapshots of one movement cycle are shown in Fig. 2(c).

Fig. 2(d) shows the setup for the robot actuation and aggregation control loop. The robots are placed on a custom-built 13-cm substrate mounted on an electrodynamic shaker, which provides the global vibration at specified combinations of amplitude and frequency. An overhead camera is installed to visually track the location of each robot in the swarm, whose degree of aggregation is then analyzed and used for adjusting the vibration parameters in real time.

One key difference between the experimental implementation presented in this paper and the theoretical studies on MIPS is the presence of boundaries of the finite substrate area. Without special treatment, robots that reach the edge of the vibrating substrate would lose motility, which results in aggregates near the boundary of the domain and interferes with the goals of this paper [38]. To minimize these *edge-effects*, we introduce a sloped region at the edge of the circular substrate. The slope is designed to smoothly return the robots reaching the edge back to the center flat region using gravitational force. This treatment greatly prevents unwanted clustering near the substrate boundary during experiments.

[2]Also see the video attachment part I.

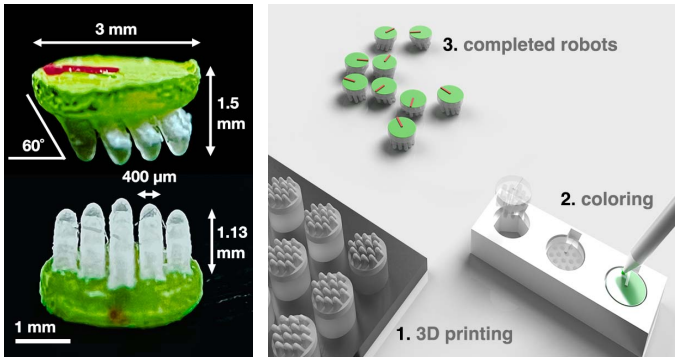

(a) (b)

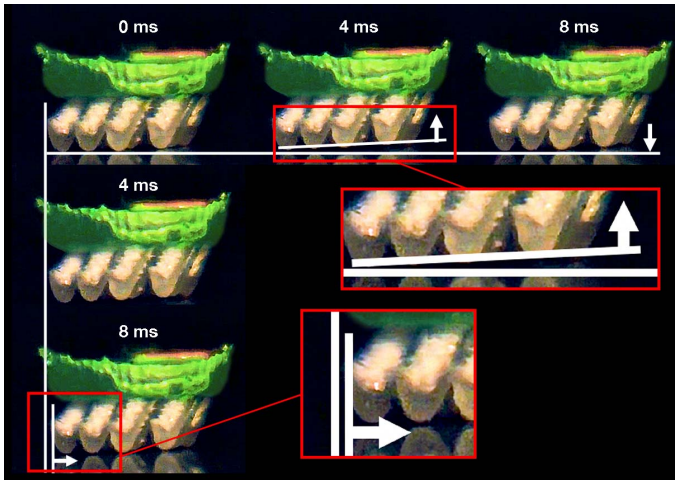

(c)

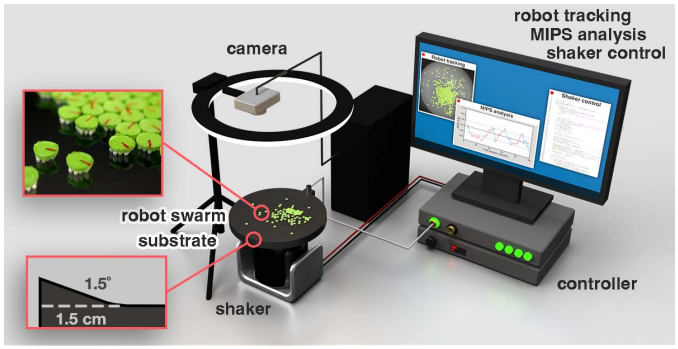

(d)

Fig. 2. Micro bristle-robot design, fabrication, locomotion, and experimental setup. (a) Robot dimensions. The robot has a circular body with a diameter of 3 mm. The bristles have a diameter of 400 μm and a tilt angle of 60° relative to the horizontal plane. (b) Robot fabrication process. (c) Frames from high-speed camera video showing hopping locomotion of the robot. Three consecutive shots showed the robot's bristles leaving the ground after collision with the vibration surface and the resulting net displacement in the forward direction. The body of the robot is partially false colored for better illustration. (d) Actuation and aggregation control system. The center of the substrate has a 10-cm flat region. The sloped region at the edge of the substrate is 1.5 cm wide and sloped at 1.5° as shown in one of the insets.

Together with the micro bristle-robots—whose motility characteristics will be discussed in Section III—the actuation and control setup provide an excellent experimental platform for studying the MIPS aggregation behaviors in the vibration driven robot swarms.

III. Motion Model

Motility-induced phase separation—defined as the spontaneous organization of self-driven particles into slow-moving dense clusters and fast-moving low-density regions—is not only closely linked with the motility characteristics of the individuals in the swarm, but also to the physics of their interactions [26]. In this section, we introduce a mathematical model to describe the motion of individual robots and their collisional interactions. In particular, we experimentally demonstrate how parameters within this motion model can be systematically varied using the vibration inputs applied to the vibration substrate.

As described in the previous section, the micro bristle-robots are designed to move in the bristles' tilt direction. With the ultimate goal of facilitating systematic control of the motion of the micro bristle-robots, we now present a kinematic model to describe the motion characteristics of the robots and their interactions with each other. The model is based on three key observations regarding the motion of the robots, as described below.

First, the hopping motion allows for a small but random change in the orientation of each robot during every hop. Due to this effect, the robots move with a near-constant speed but experience a slow stochastic diffusion on their orientation. This type of motion is characterized via a well-known stochastic differential equation, known as the Langevin equation [39], which can be parameterized by the linear speed of the robot v_0 and the rotational diffusion coefficient D_r which affects the rate of orientation change.

Second, when the robots collide with each other, they experience a slow-down due to the normal forces generated during the collisions. Meanwhile, each robot i also experiences a frictional force f_i on its rotational motion, which changes based on the number of robots it collides with.

Third, as a robot enters the sloped region on the edge of the domain (see Fig. 2(d) inset), it experiences both translational and rotational effects, symbolized by $s_{t,i}$ and $s_{r,i}$, respectively, in (2)–(7). These values are parameterized by $L \in [0, 1]$, a dimensionless parameter which represents the effect of the slope of the substrate on the motion of the robots.

For a team of N robots, let $z_i(t) = (x_i(t), y_i(t))$ and $\theta_i(t)$ denote the position and orientation of robot $i \in \{1, \ldots, N\} \equiv \mathcal{N}$ at time t, respectively. Each robot has a circular footprint of radius r and operates in a closed and bounded domain $\mathcal{D} \subset \mathbb{R}^2$. With the aim of mathematically modeling the kinematics of the micro bristle-robots, we let $\mathcal{D}$ be a circular planar region with an annular set $\Delta\mathcal{D} \in \mathbb{R}^2$ surrounding it, where additional forces are added to the robots to account for the sloped vibration surface of the domain. Let $\mathbb{N}_i(t)$ denote the set of robots that robot i is colliding with at time t, and $N_i(t)$ denote its normalized cardinality, defined as

$$N_i(t) = \frac{|\mathbb{N}_i(t)|}{N_{\max}} \tag{1}$$

where $N_{\max}$ is the maximum number of robots that a given robot can collide with simultaneously, as allowed by robot geometry. In the case of micro bristle-robots which have a circular footprint and operate on a planar surface, this normalization constant is $N_{\max} = 6$ [40].

The kinematics of the micro bristle-robots can then be represented using the following modified Langevin dynamics (see [29], [41] for further reference):

$$\dot{x}_i = \left(v_0 \cos\theta_i + \mu \sum_{j \in \mathbb{N}_i} f_{cx}\left(x_i - x_j\right) \right) s_{t,i} \tag{2}$$

$$\dot{y}_i = \left(v_0 \sin\theta_i + \mu \sum_{j \in \mathbb{N}_i} f_{cy}\left(y_i - y_j\right) \right) s_{t,i} \tag{3}$$

$$d\theta_i = \left(\sqrt{2D_r}\Delta W_\theta \right) s_{r,i} f_i \tag{4}$$

$$s_{t,i} = \begin{cases} (1 - L) \text{ , if } z_i \in \Delta\mathcal{D} \\ 1, \text{ otherwise} \end{cases} \tag{5}$$

$$s_{r,i} = \begin{cases} (1 - L)\, \frac{\pi}{2} \sin\left(\theta_i - \tan^{-1} \frac{y_i}{x_i} \right) \text{ , if } z_i \in \Delta\mathcal{D} \\ 1, \text{ otherwise} \end{cases} \tag{6}$$

$$f_i = 1 - \frac{F\beta N_i}{1 - (1 - \beta)\, N_i}, \tag{7}$$

where ΔW_θ denotes the Wiener process increment representing white Gaussian noise [42]. The friction value f_i in (4) is parameterized by the friction non-linearity coefficient β and the maximum friction magnitude F. It is worth mentioning that there is no need to account for friction in the linear velocity of the robots, as the latter decreases as a result of the inter-robot collisions. The motility parameter μ enables the use of collisional forces f_{cx} and f_{cy} in the kinematic equations directly. For $f_{cx}\left(x_i - x_j\right)$ and $f_{cy}\left(y_i - y_j\right)$, the following inverse law is used [43]:

$$f_{cx}\left(x_i - x_j\right) = \frac{x_i - x_j}{\sqrt{(x_i - x_j)^2 + (y_i - y_j)^2}}, \tag{8}$$

$$f_{cy}\left(y_i - y_j\right) = \frac{y_i - y_j}{\sqrt{(x_i - x_j)^2 + (y_i - y_j)^2}}, \tag{9}$$

where $x_j \in \mathbb{N}_i$ or, equivalently, $x_i \in \mathbb{N}_j$. The parameter L in the expression of $s_{t,i}$ and $s_{r,i}$ is used to tune the effect of the sloping boundary on the linear and angular speeds.

In order to validate the suitability of the model (2)–(7) at capturing friction and boundary effects, we developed a simulator that leverages the parallel computation capabilities of graphics processing units to simulate a large number of physically interacting particles. The parameters of the modified Langevin dynamics to account for friction effects (i.e., F and β) have been tuned using simulation data. A similar data-driven approach has been employed to estimate the parameter L which is used in (5) and (6) to characterize the magnitude

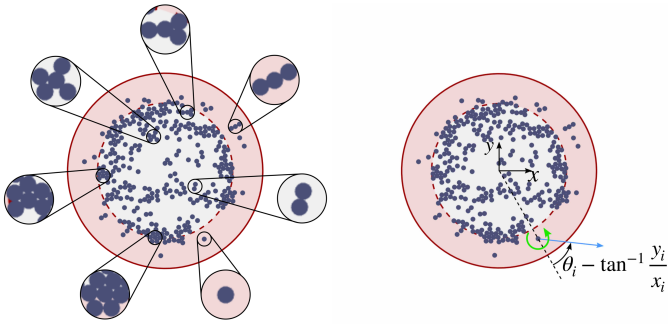

(a) (b)

Fig. 3. Friction and edge effects in the multi-bristle-robot simulator. The robots (blue dots) move on a circular substrate depicted as a gray-shaded region, where the red annulus denotes the sloped region. In 3(a), seven different conditions are highlighted where a robot is surrounded by 0 to 6 robots, respectively (i.e., $N_i = 0, \ldots, 6$). The effect of friction is captured by the scaling factor f_i in (4) that reduces the angular velocity of a robot when in contact with other robots, as a function of the number of neighboring robots N_i. The effect of sloped edges is introduced by means of a scaling factor $s_{r,i}$ on the angular velocity $\dot{\theta}_i$ proportional to the misalignment of the robot (whose orientation is depicted in light blue in 3(b)) with respect to the radial direction (shown as a dashed black line). This misalignment is represented by the quantity $\theta_i - \tan^{-1}(y_i/x_i)$ in 3(b) and in (6). This effect is depicted as a green arrow representing an additional angular velocity oriented towards the downhill direction. Additionally, the scaling factor $s_{t,i}$ reduces the linear velocity to simulate the reduced effectiveness of vibrations to produce locomotion.

of the edge effect in terms of reduction of robot linear and angular speed by the scaling factors $s_{t,i}$ and $s_{r,i}$, respectively. Fig. 3 pictorially shows how the friction and edge effects are simulated. On the other hand, v_0 and D_r are estimated using data collected from micro bristle-robot experiments.

A convenient metric to measure the motility of individual robots is the *activity* parameter [41], A, which is proportional to the distance traveled by a robot before its direction uncorrelates completely,

$$A = \frac{v_0}{2rD_r}, \tag{10}$$

where r is the radius of the robot. Alternatively, this parameter (measured in units of rad^{-2}) can be interpreted as being inversely proportional to the diffusivity of the robot's orientation θ, normalized by the distance traveled by the robot—measured in body lengths—over a fixed interval of time.

Fig. 4(a)-4(c) sweep the vibration parameters (amplitude and frequency) experimentally to demonstrate how the motility characteristics–v_0, D_r, and A–of the individual robots can be modified. A total of 50 different amplitude and frequency combinations are tested. Multiple robots are tested for each condition, and the average result is reported. (For a complete table of swept vibration parameters, motility characteristics, and number of robots tested, please see Table II.) In the rest of the paper, we present results by applying 5 distinct amplitude and frequency input combinations out of the 50. For convenience, these conditions are summarized in Table I. Owing to variabilities in the construction of the robots, as well as minute variations in the surface, the motility parameters of individual robots can vary. Fig. 4(d) shows the variance in the motility parameters of 20 robots individually tested under vibration settings #1 to #3. Examples of individual robot trajectories generated under these different settings are shown Fig. 4(e)[3].

TABLE I
FREQUENCY AND AMPLITUDE OF SELECTED VIBRATION CONDITIONS

Condition	Frequency (Hz)	Amplitude (mm pk-pk)
#1	300.00	0.0110
#2	300.00	0.0138
#3	300.00	0.0193
#4	239.32	0.0179
#5	350.32	0.0124

As seen in Fig. 4, the vibration inputs supplied to the vibrating substrate enables us to control both the linear as well as rotational motion characteristics of the robots. As described in Section IV and Section VI, both parameters are intricately linked with the ability of the robots to form and maintain high density clusters when operating together.

IV. Characterizing Inter-robot Collisions

In this section, we investigate and experimentally characterize the inter-robot phenomenon fundamentally responsible for motility-induced phase separation in a swarm of colliding micro bristle-robots. This phenomenon relates to the variations in the speed of an individual robot as a function of the local density of robots around it. The results presented in this section serve a threefold purpose: *(i)* they highlight the mechanisms underlying the observed aggregation characteristics in the rest of this paper, *(ii)* they highlight significant deviations between the speed-density relationships observed in the micro bristle-robots and those observed in typical active matter studies, and *(iii)* they provide insight into the source of such deviations. These insights ultimately enable the closed-loop control of swarm aggregation in Section VI.

For a team of colliding robots, the average speed reduces with the increasing density of the region—a direct consequence of density-dependent collision rates [44]. To verify this hypothesis, we collected the time-stamped instantaneous robot speeds and the local robot density in a swarm of 225 robots (tested for three different vibration settings, with an experiment duration of 5 minutes and data sampling rate of 30 Hz). The collected data was binned and averaged over the 225 robots. Towards this end, Fig. 5(a) plots the average instantaneous robot speed in the swarm of 225 robots as a function of the local robot density, tested for three different vibration settings. The swarm size was chosen to reflect a scenario where the density was high enough to cause significant slowdown of robots but not too high to precipitate phase separation which might distort the speed-density data [41].

The local density is characterized by a smooth field which is computed in the following manner. We divide the region $\mathcal{D}$ into a grid using l^2 lattice points. Let $\mathcal{W}(p, s, w)$ denote a square region centered around grid point (p, s) and with

[3]Also see the video attachment part II.

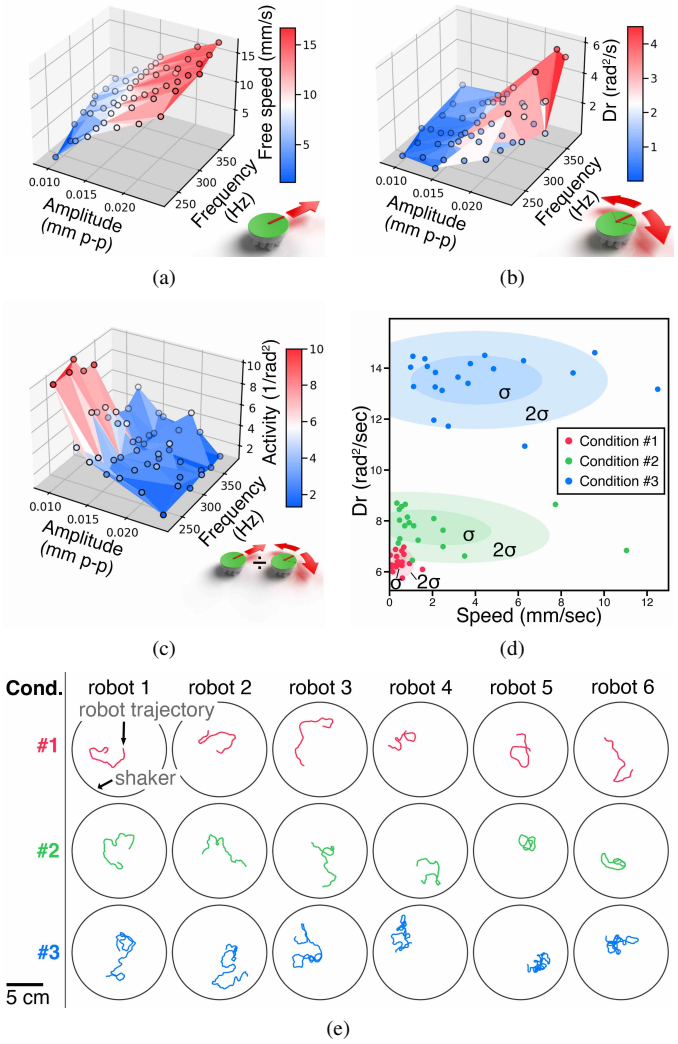

Fig. 4. Experimental characterizations of motility characteristics of individual robots. (a) Robot speed v_0, (b) rotational diffusion coefficient D_r, and (c) activity A measured for different vibration frequencies and amplitudes. Each data point in (a)-(c) is averaged across multiple robots, where the number of robots tested for each condition is indicated in Table II. In (c), the data is capped at 10 rad^{-2} for illustration purposes. (d) Variation in the motility parameters of the randomly selected individual micro bristle-robots (speed v_0 and rotational diffusion coefficient D_r) under different vibration settings. The shaded area depicts the 1- and 2-standard deviation ellipses computed from the obtained data. (e) Individual robot trajectories generated from the characterization tests illustrate the variations in the motility characteristics of the robots, the effect of different vibration settings, and the inherent stochasticity in the motion of the robots.

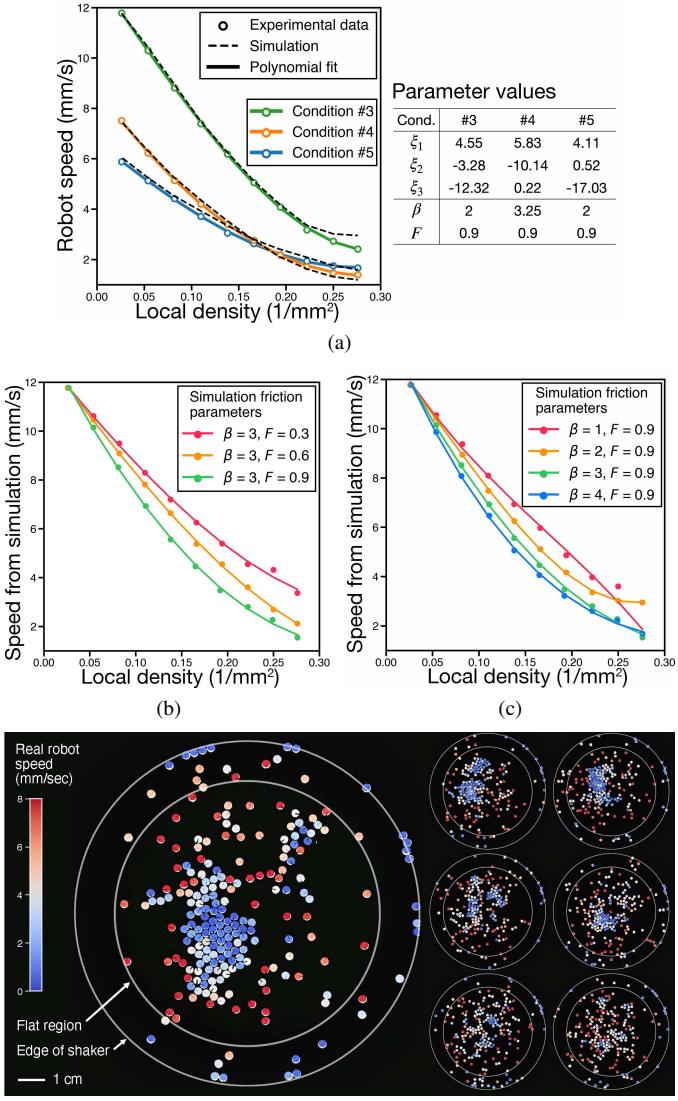

Fig. 5. The collision-induced slow-down of robots precipitates high-density aggregate formation. (a) Experimental average instantaneous robot speeds vs. local robot density in a swarm of 225 colliding micro bristle-robots. The best polynomial fit along with the corresponding result from simulations are also depicted. (b) Simulated instantaneous speed vs. local robot density curves, for varying values of friction magnitude parameter F. (c) Simulated instantaneous speed vs. local robot density curves, for varying values of friction non-linearity parameter β. (d) Experimental snapshots of the speed-density characterization experiments under condition #4. The speeds of robots are represented by the color overlay, where red and blue correspond to high and low speed, respectively.

side length w. The coarse-grained density computed over the region with windowing size w at time t is then defined as,

$$[\lambda_w(t)]_{p,s} = \frac{|\{z_i(t) : z_i(t) \in \mathcal{W}(p,s,w)\}|}{|\mathcal{W}(p,s,w)|}, \qquad (11)$$

for $(p,s) \in \{0,1,\ldots,l-1\}^2$. The notation $|S|$ is used to denote the measure of the set S, so that the numerator of (11) is equal to the number of robots located within the window $\mathcal{W}(p,s,w)$, while the denominator is the area of the window itself. For data collected from each physical experiment, we also plot a best-fit third-order polynomial which captures the relationship between the local density and speed of the robots ($w = 6$ mm):

$$v(\lambda_w(t)) = v_0\left(1 - \xi_1\lambda_w(t) - \xi_2\lambda_w^2(t) - \xi_3\lambda_w^3(t)\right), \qquad (12)$$

where the parameters (ξ_1, ξ_2, ξ_3) are chosen to best fit the observed data in the least-squares sense.

The distinctly non-linear speed-density relationship captured in Fig. 5(a) can be contrasted against the linear decay models observed in simulated active Brownian particle swarms [29], [41]. To individually measure the effects of the various factors which differentiate our swarm platform from idealized particles, we built a simulator to mimic the motion

characteristics of the micro bristle-robots, their collisional interactions, and the effects of the sloping edges of the vibrating platform (Also see Appendix B). Fig. 5(b)-5(c) plot the speed-density relationship obtained in a simulated swarm of 225 robots (each simulation lasted 5 minutes and speed/density data was collected at 30 Hz) for varying values of the friction non-linearity parameter β and maximum friction magnitude F described in (7). As seen, these factors have a significant effect on the curvature and slope of the speed-density relationship, indicating the non-trivial role played by rotational friction in the micro bristle-robot collisions. In particular, increasing values of β and F decreases the slope of the speed-density curves, thus increasing the propensity of the robots to form aggregates. We hypothesize that this is a major contributor to the significant deviations—between collision-based slow-down in idealized active matter particles and micro-bristle robots—discussed at the beginning of this section. The results of the polynomial parameters (ξ_1, ξ_2, ξ_3) and simulated friction parameters (β, F) chosen to match the speed-density relationships obtained from experimental data are summarized in the inset table in Fig. 5(a), and the simulated response is plotted in Fig. 5(a) against the experimental data as well.

Fig. 5(d) overlays the instantaneous speed information of the robots on snapshots of the conducted experiments and illustrates how the density-dependent slowing down of robots is both a cause and a consequence of the formation of high-density robot aggregates (leading to a positive feedback effect)[4]. As seen, slow moving robots are found primarily in high-density clusters, which tend to grow when fast-moving robots collide with them.

Leveraging these characterizations of individual robot and swarm behavior, the following sections develop a mechanism to control the extent to which aggregations occur among colliding micro bristle-robots. We first introduce a novel metric to quantify the extent of aggregation, which ultimately allows us to design control mechanisms to manipulate the behavior of the swarm as a whole. For the rest of this paper, we use the parameters $(\mu = 30, L = 0.25)$ when simulating the motion of the robots.

V. The MIPS Index

In this section, we introduce the *MIPS index*, a novel metric for evaluating the extent of robot aggregation occurring in the environment, and compare it against an existing method for quantifying aggregation. This condensed representation of the current aggregation state of the swarm ultimately enables its regulation and control in Section VI.

A. Definition

The MIPS index is based on the computation of densities as given in (11), however, the resulting metric is independent of the window size $\mathcal{W}(p, s, w)$. This is an advantage over existing approaches—such as clustering analyses based on adjacency relations [45], density-based clustering [46], and sampling-based methods [47]–[49]—as (i) it is able to reliably capture the phenomenon of phase separation in a swarm, and, more importantly, (ii) it does so without requiring any a posteriori manual parameter tuning based on the observed behavior of the robots.

Towards this end, let $\mathrm{Var}(\lambda_w)$ denote the variance of the density distribution over the domain for a given window size w, i.e.

$$\begin{aligned}\mathrm{Var}(\lambda_w) =& |\mathcal{D}|^{-1} \sum_{(p,s)\in\{0,1,\ldots,l-1\}^2} [\lambda_w]^2_{p,s} \mathrm{d}p\mathrm{d}s \\ &- \left(|\mathcal{D}|^{-1} \sum_{(p,s)\in\{0,1,\ldots,l-1\}^2} [\lambda_w]_{p,s} \mathrm{d}p\mathrm{d}s \right)^2,\end{aligned} \tag{13}$$

where $[\lambda_w]_{p,s}$ is defined in (11) and $|\mathcal{D}|$ is the area of set $\mathcal{D} \subset \mathbb{R}^2$. In order to build a metric which is independent of the window size $\mathcal{W}(p, s, w)$ used in the computation of the density field, we average the variance of density $\mathrm{Var}(\lambda_w)$ over an interval of window sizes $[w_{\min}, w_{\max}]$, as follows:

$$I_A = \frac{\int_{w_{\min}}^{w_{\max}} \mathrm{Var}(\lambda_w) \mathrm{d}w}{w_{\max} - w_{\min}}, \tag{14}$$

where the subscript A explicitly encodes the dependence of the calculated MIPS index on the activity parameter (defined in (10)). Fig. 6(a) illustrates the operations involved in the computation of the MIPS index. At the top, the windowing-based density computations presented in (11) are depicted. Each of the convolution operations employs a different window size w for the computation of the coarse-grained density field λ_w (11) at varying levels of granularity. At the bottom left, the graph of the variance of these density fields (13) is shown as a function of the window size. The average of density variance I_A is calculated. Finally, at the bottom right of the figure, the value of MIPS index is obtained by normalizing I_A against maximum and minimum values possible for a specific setup, which will be discussed later.

It is worth pointing out that while different windowing region shapes (e.g., circular) can be utilized for the MIPS index computation, the usage of the square window $\mathcal{W}(p, s, w)$ presents a computational advantage. This is primarily because the window can then be defined as a Cartesian product of x- and y-bounds, leading to a faster evaluation of (11).

The range of values attainable by an index characterizing the phase separated behavior depends on the size of the environment, the size of the robots, and the average swarm density. For example, a circular cluster of a given diameter corresponds to a distinct phase separated behavior if the cluster is in the middle of a much larger environment. On the other hand, if the circular cluster is placed in a square environment whose side is equal to the cluster diameter, the configuration is much closer to uniformly spread rather than being phase separated. In summary, the phase separation behavior we are interested in characterizing through the MIPS index should be agnostic of robot and environment sizes. Therefore, we define the MIPS index by normalizing I_A in (14) in such a way

[4]Also see the video attachment part III.

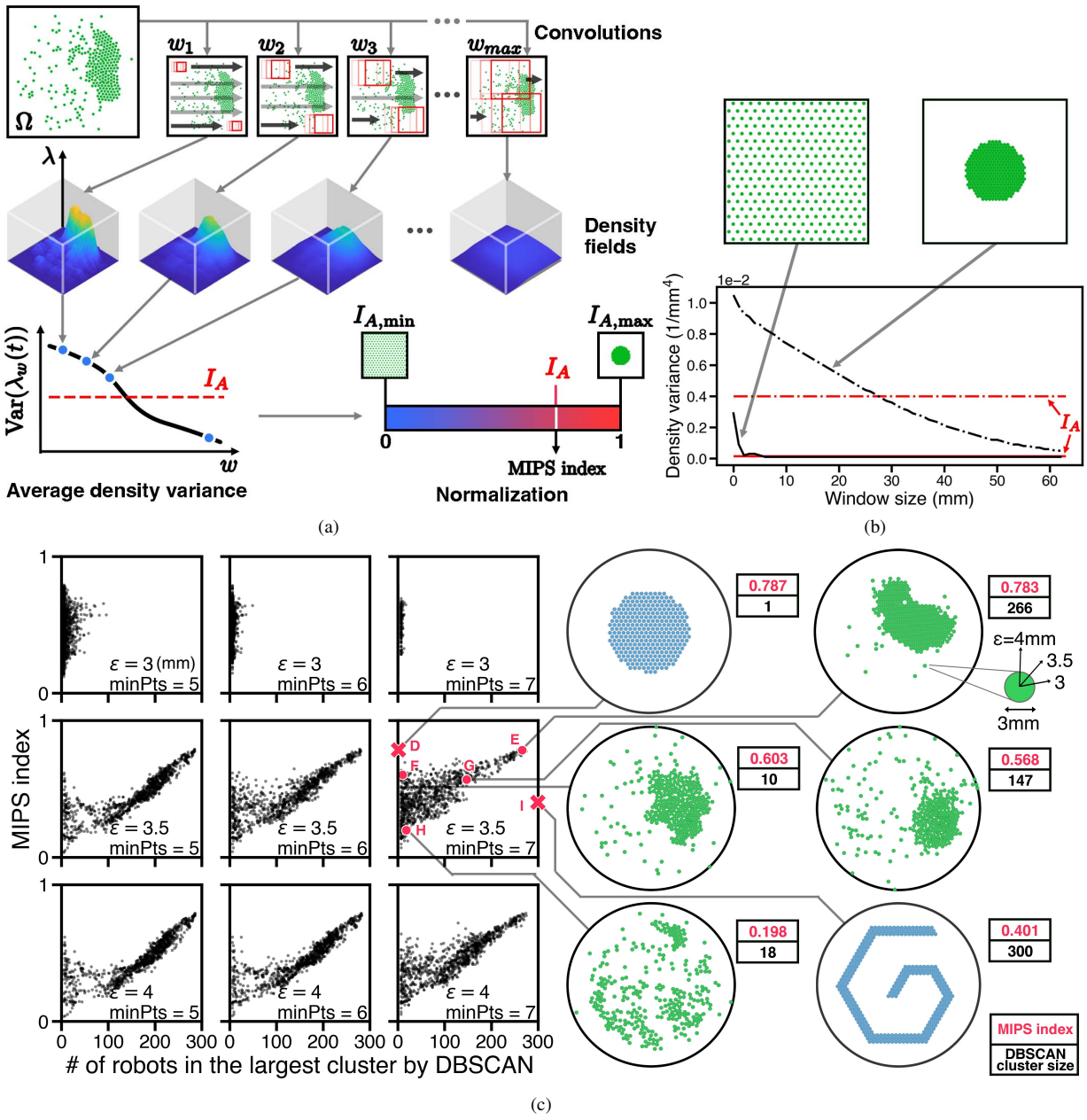

Fig. 6. MIPS index computation and comparison against DBSCAN. (a) MIPS index computation procedure. First, multiple runs of convolutions are performed with varying window sizes, providing different density fields. Second, the variances of each density field are computed. Lastly, the MIPS index is calculated as the normalized average of variances over window sizes. (b) Quantitative evaluation of the MIPS index for the two opposite scenarios of uniform density and circle packing of 300 robots in a square environment. The MIPS index in the first case is extremely low, clearly indicating the uniformity of the distribution of the robots in the environment. In the second case, instead, a significantly higher MIPS index characterizes the smallest cluster that the same number of robots can achieve, fully capturing, this way, the phase-separated robotic swarm. (c) MIPS index vs. DBSCAN result (number of robots in the largest cluster). A collection of 1000 sets of 300-robot swarm position data were generated through CUDA simulation. The data was analyzed by MIPS index calculation and DBSCAN with different values for parameters ϵ and minPts. Green swarms are selected from simulated experiments with high, medium, and low MIPS indices and DBSCAN results are shown on the right. Two artificial extreme scenarios (blue swarm) where MIPS index disagrees with DBSCAN result also shows that MIPS index can capture the global density variance better.

that the minimum and maximum attainable values, $I_{A,\min}$ and $I_{A,\max}$, correspond to the values 0 and 1 of the MIPS index:

$$\text{MIPS index} = \frac{I_A - I_{A,\min}}{I_{A,\max} - I_{A,\min}}. \tag{15}$$

As mentioned above, the values of $I_{A,\min}$ and $I_{A,\max}$ depend on size of environment and robots, and the number of robots. In Fig. 6(b), an illustration of the robot configurations for which we want the MIPS index to attain a value of 0 (top left) and 1 (top right) are reported.

B. Quantifying Phase Separation

The ability of the MIPS index to capture phase separation behaviors can be inferred by considering the examples of Fig. 6(b). In the case depicted at the top left, a non-phase-separated swarm of robots is depicted together with

the variance of densities computed for window sizes ranging from $w_{\min}$ equal to the robot diameter, to $w_{\max}$ equal to the environment size. As can be seen, since the distribution of robots is closer to uniform in non-phase-separated cases, the average variance of density (i.e., the MIPS index) is low. In the case shown at the top right of Fig. 6(b), on the other hand, a phase-separated robot configuration leads to a high MIPS index. In fact, in this scenario, significant variations of density across the robot domain can be observed. Therefore, the variance of density is higher compared to a uniform distribution of robots. Moreover, as the window size used to compute the density field increases, these variations do not attenuate as rapidly as they do in the case of non-phase-separated cases. As a result, the average variance of density will be higher.

With the aim of showing the advantage of the MIPS index over traditional cluster analyses tools, we now report the results of comparisons between the MIPS index and the size of the largest cluster in the swarm, obtained through the Density-Based Spatial Clustering of Applications with Noise (DBSCAN) algorithm, as an estimation of the aggregation level [46]. The latter is based on two parameters, ϵ and minPts, representing, respectively, the maximum distance between two robots in order to define them as neighbors and the number of neighboring robots needed to classify a robot as belonging to a cluster. Fig. 6(c) shows the correlation between the MIPS index and largest cluster obtained using DBSCAN for a variety of robot configurations recorded during the course of simulated experiments. For a given choice of parameters required by DBSCAN, the MIPS index captures the maximum cluster size (bottom row in Fig. 6(c)). Nevertheless, for different choices of parameters, the largest cluster size computed by DBSCAN can vary arbitrarily, decreasing to values much smaller than 100, as shown in the top row. Two artificial swarm distributions (plotted in blue in Fig. 6(c)) highlight the suitability of the MIPS index over the maximum cluster size in capturing phase-separated robotic swarms. In the upper left plot, a phase-separated robotic swarm is depicted: as expected, the MIPS index is high, while, employing the DBSCAN algorithm can lead to a maximum cluster size equal to 1—no robot is considered in the same cluster with others since the distance between any two adjacent robots is slightly greater than the minPts parameter of DBSCAN. On the contrary, the bottom right plot shows a specific example of a non-phase-separated robotic swarm configuration. Although the density is not uniform, there is no clear aggregation behavior within the circular domain. This is reflected in a low MIPS index (about half of the one attained for the other artificial swarm). Employing the same parameters chosen for the previous case, the resulting maximum cluster size obtained using DBSCAN is 300—the whole swarm is considered one big cluster.

To summarize, traditional cluster analysis methods such as DBSCAN require parameter tuning and manual visual inspections in order to obtain the expected results in characterizing phase separation. Instead, we have shown how the MIPS index introduced in this section works better to effectively capture phase separation phenomena for it provides reliable results across diverse scenarios.

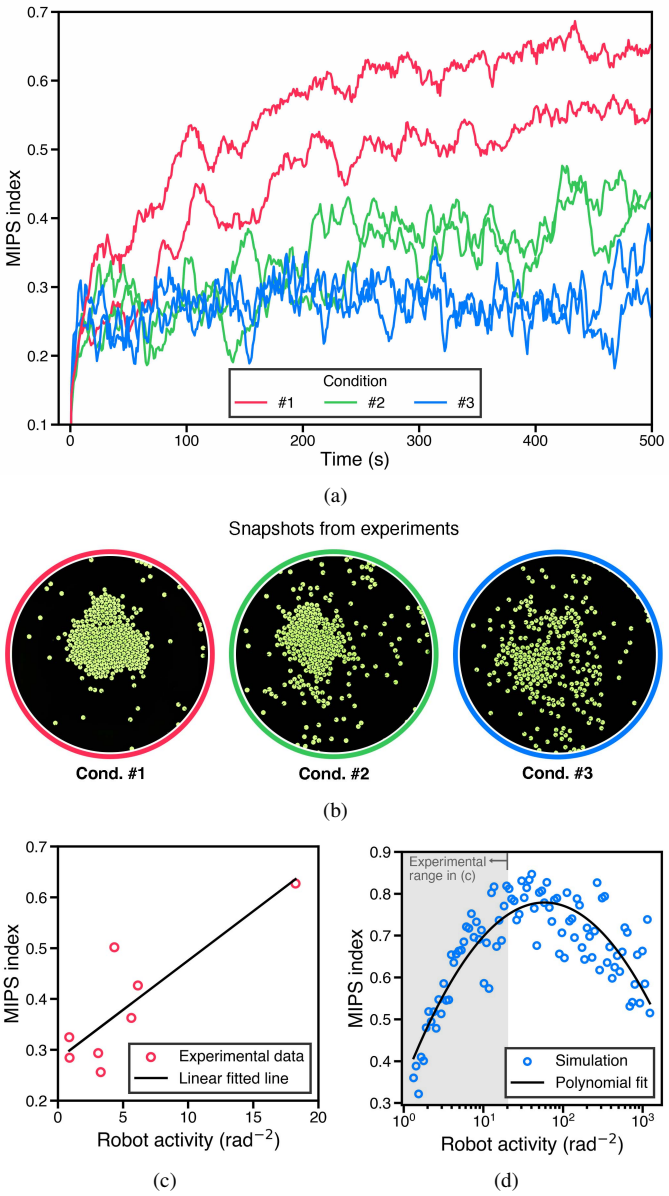

Fig. 7. Open-loop aggregation results of the micro bristle-robot swarm under different vibration conditions. (a) MIPS index trajectories under vibration conditions #1 to #3. Different levels of equilibrium MIPS indices can be achieved by different vibration conditions. For each condition, two trajectories are shown in the figure. (b) Snapshots from different experiments in (a) after the swarm has reached equilibrium. (c) Experimental MIPS index at equilibrium vs. robot activity plot under 8 different vibration conditions tested. A line is fitted to the data. (d) Simulated equilibrium MIPS index vs. robot (log scale) activity plot. A polynomial line is fitted to the data to illustrate the trend. The shaded area represents the activity range experimentally tested in (c). The decrease of MIPS index at high robot activity values can be attributed to secondary effects, such as bouncing and lateral motion, which become more prominent during collision between robots moving at higher speeds.

VI. Aggregation Behavior and Control

As discussed in Section IV, robots in the swarm experience a density-dependent variation in their speeds as they move through the domain. This is the precondition for MIPS to occur, where aggregates form because slow moving clusters precipitate further accumulation of robots leading to a run-away effect. It is also shown that a wide range of motility characteristics of micro bristle-robots (v_0, D_r) can be achieved

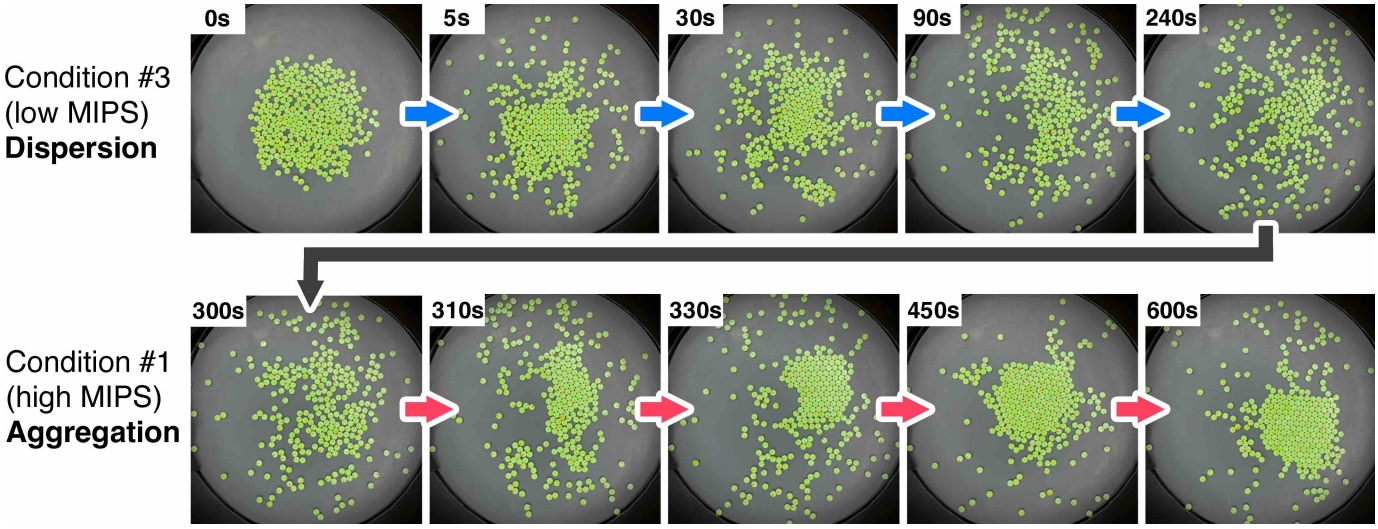

Fig. 8. Experimental results of dispersion and aggregation of the 300-robot swarm under condition #3 (low MIPS) and #1 (high MIPS), respectively.

by varying vibration parameters (frequency and amplitude) of the vibrating substrate. In addition, the newly introduced MIPS index serves as a metric to quantify the extent of aggregation within the swarm. In this section, we present both the *open-loop* aggregation behaviors in a swarm of approximately 300 micro bristle-robots and how we target specific levels of aggregation with a *closed-loop* bang-bang control system.

A. Open-loop Aggregation Behaviors

To determine a set of vibration modes that can achieve a wide range of aggregation levels and study the intrinsic aggregation behaviors under these modes, the swarm is first put under multiple constant vibration conditions. As shown in Fig. 7(a), three conditions (#1, #2, and #3 in Table I) are determined as the main vibration modes of the swarm, which give rise to MIPS index at three distinct levels–high, medium, and low, respectively. The 300-robot swarm is tested with each of the three conditions starting from an approximately uniform distribution. The MIPS index of each vibration condition reaches equilibrium under the prolonged actuation, and modes corresponding to larger MIPS indices require longer time. The actual swarm distributions under each condition and under equilibrium are shown in Fig. 7(b). Visually, the swarm shows different levels of aggregation under different conditions, in agreement with the MIPS index trajectories[5]. The average MIPS indices under equilibrium span from 0.24 to 0.57, which is 33% of the full range defined by the extreme cases used for normalization. This result verifies the idea of using MIPS to reach different levels of aggregation by controlling robot motility characteristics.

The experimental and simulated open-loop equilibrium MIPS indices under various conditions are plotted against robot activity (A) in Fig. 7(c) and 7(d), respectively. In the activity range tested, $0.88 \leq A \leq 18.25$ rad^{-2}, the combination of experimental and simulation results verifies the dependency discussed earlier, as the system has a general trend of having more aggregation and thus larger equilibrium MIPS index under conditions where the robot activity is higher. In addition, the simulation result in Fig. 7(d) is plotted over a wider range of robot activity. It shows how the relationship extends beyond what is experimentally achievable, where the trend inverts for high values of robot activity, A.

Fig. 8 demonstrates the swarm's capability to reach different levels of aggregation when sequentially actuated with different modes[6]. Starting from an initial cluster, when presented with vibration condition #3, which corresponds to low equilibrium MIPS index values in the open-loop experiment, the cluster quickly dissolves, and robots are distributed to different parts of the domain. When the vibration condition is switched to #1, which corresponds to a high MIPS index, the swarm gradually forms a large cluster again. What we see here is the opportunity to use only two modes, one associated with the low equilibrium MIPS index and one with high, to control the instantaneous MIPS index and move it in either increasing or decreasing direction regardless of current aggregation status as long as it is between what can be achieved by the two.

B. Closed-loop Aggregation Control

To explore this idea, we build a closed-loop control setup with a bang–bang controller which switches between the two modes mentioned above. The MIPS index is calculated based on real-time robot positions every second, and the control input switches between condition #1 and #3 when the value hits the upper and lower tolerance boundaries. Fig. 9(a) shows the experimental result of this with a target MIPS index of 0.29 ± 0.05. As shown, the aggregation level is successfully stabilized to a constant MIPS index value within a margin that is close to the commanded tolerances. It is noticeable that there are overshoot and undershoot on each side of the tolerance boundaries. These variations stem from each individual robot's stochastic motion. It is also observed that it takes longer for condition #1 to raise the MIPS index than using condition #3

[5]Also see the video attachment part IV.

[6]Also see the video attachment part V.

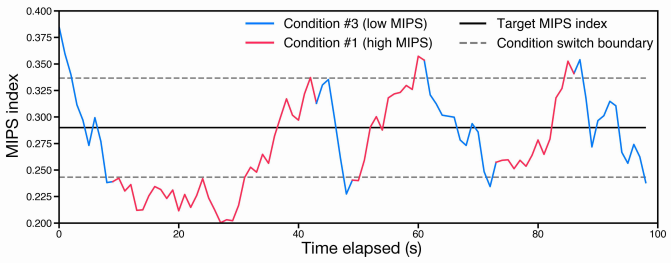

(a)

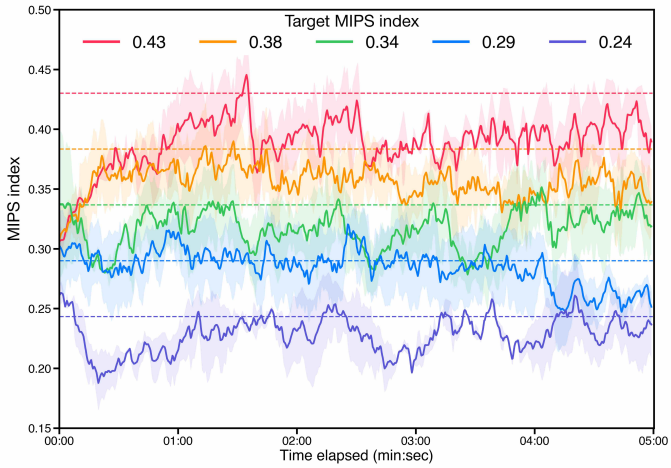

(b)

Fig. 9. Closed-loop aggregation control of the robot swarm with two vibration modes. (a) Experimental result of the closed-loop control with a bang-bang controller, which uses condition #3 and #1 as low and high control inputs to confine the MIPS index value in 0.29±0.05. The vibration condition switches when the real-time MIPS index value hits the tolerance boundaries. The line color corresponds to the segments under each one of these two vibration conditions. (b) Averaged MIPS trajectories ($N = 3$) when using the controller to control the MIPS index to achieve multiple levels from 0.24 to 0.43. The shaded area represents the standard error of the averaged MIPS index across multiple runs.

to lower the MIPS index, which is due to the speed difference under these two conditions.

In addition, we controlled the swarm to target various MIPS indices spanning from 0.24 to 0.43. Each time, the controller is programmed to immediately switch between vibration modes when the current MIPS index is higher or lower than the target. The resulting averaged MIPS index trajectories are shown in Fig. 9(b)[7]. Though with significant fluctuations caused by system stochasticity, the experiments show distinct MIPS index bands corresponding to different levels of aggregation. The effect of robot speed difference, which leads to the faster decrease and slower increase of the MIPS index, is more pronounced at higher MIPS indices because the clustering dynamics are slower for the chosen conditions. The closed-loop results demonstrate how the aggregation level can still be controlled with a limited set of vibration modes, which can be useful in situations where the ranges of vibration parameters are constrained.

Both open-loop and closed-loop experimental results confirm the viability of controlling collision-induced aggregation of the micro bristle-robot swarm by globally changing the motility characteristics of individual robots.

[7]Also see the video attachment part VI.

VII. Conclusion

In this paper, we presented a closed-loop collision-based aggregation control in a swarm of sensorless micro bristle-robots, as well as the first large-scale realization of motility-induced phase separation (MIPS) behaviors on a swarm robotic platform to the best of the authors' knowledge. The vibration-driven robots were designed to react in a predictable fashion to the global control inputs (vibration amplitude and frequency) and demonstrated variable motility behaviors, making them ideal specimens for the study. Though each individual robot's motion cannot be precisely controlled, the swarm as a whole presents different degrees of aggregation under various vibration conditions. In addition, we proposed the MIPS index as a novel metric to quantify the aggregation behavior based on the variance in the density fields. It was shown that regardless of the inherent stochasticity of the system arising from the dynamics of the robots, the aggregation characteristics of the swarm can be controlled through real-time feedback.

The mathematical models, characterization experiments, and setup provide a pipeline for future studies of minimally equipped micro-robot swarms where interactions among individual robots and with the environment can induce emergent swarm behaviors. Future works include: (i) Generalization and adaptation of the findings in this paper to other robotic swarms and applications, where the robot interactions can entail physics of other kinds, such as magnetic and acoustic forces; (ii) Investigations of using spatially-varying vibration fields to control the swarm's centroid movement and density distribution. Furthermore, by designing robots that can respond to environmental signals of interest, which induce local motility variations, the same concept can achieve applications such as environmental monitoring and targeted drug delivery.

Acknowledgments

The authors thank the GVU Prototyping Lab at Georgia Institute of Technology for providing high-resolution 3D printing capability, and Dr. David Hu and Hungtang Ko for the fire ant raft photo.

Appendix A
Materials and Equipment

The micro bristle-robots were 3D printed with material VisiJet M3 Crystal by Project 3510 HD (3DSYSTEMS). After printing, ultrasonic baths of mineral oil (McMaster-Carr) and dishwashing liquid solution were performed for removal of the wax supporting material. The top surface robot was painted green, and the orientation indicator was painted red, both with Sharpie oil-based paint markers.

The shaker system consists of an ET-126HF electrodynamic shaker (Labworks), a VR9500 vibration controller (Vibration research), a PA-138-1 power amplifier (Labworks), and a customized substrate 3D printed by Form 3 (Formlabs), which has a flat center region of 10 cm in diameter and a peripheral sloped region with a extend of 1.5 cm. A monitoring

accelerometer (Labworks, 105-00008) was mounted on the top of the substrate. The vibration controller was interfaced with MATLAB and thus the shaker vibration frequency and amplitude can be programmed/controlled in real-time. A custom-built Python program was used to detect robot locations and orientations of the whole swarm based on the video feed captured by overhead webcam (Logitech, C615). Location information was used to calculate the MIPS index in MATLAB. The MIPS index value was then used for adjusting shaker vibration parameters.

For more details on robot tracking program, please see Appendix C.

APPENDIX B
CUDA SIMULATOR

The multi-micro-bristle-robot simulator has been implemented to be deployed on a graphics processing unit (GPUs). Computational threads are spawned in parallel on the GPU in order to calculate the interaction forces between all pairs of neighboring robots required to efficiently simulate collision dynamics. The simulator runs in a Docker[8] container, asynchronously with respect to the control and analysis scripts. The interfaces with the hardware, such as camera for robot tracking and the electrodynamic shaker, also run asynchronously with the simulator. The communication between the tracking, analysis, and control scripts with the simulator has been handled using MQTT[9], a lightweight publisher-subscriber messaging protocol. The MIPS index controller has been implemented in MATLAB, where, based on the robot positions received from the simulator, the MIPS index is evaluated, and the drift velocity v_0 and rotational diffusion coefficient D_r are computed and sent back to the simulator.

Both open-loop and closed-loop experiments conducted with the real robot swarm were repeated and simulated in the simulator as shown in Fig. 10(a) and 10(b). In the simulator, the model parameters (see Section III) were tuned to match the MIPS trajectories obtained via real robot experiments. Both simulation results show close correlation with real-life swarm behaviors, validating the effectiveness of the mathematical models and the simulator implementation. The stochastic behavior of the system, as well as the consequent overshoots and undershoots of the closed-loop controller, were also captured in the simulation results.

APPENDIX C
ROBOT TRACKING METHODS

An overhead camera is used to capture live images of the swarm. Images are fed into a custom-built computer vision program based on OpenCV library[10] to extract each individual robot's position and angle. The approaches are detailed below.

Multi-stage template matching is used for accurate robot position tracking (Fig. 11). The following steps are taken to perform it: (1) Initialize a high threshold (α_0). (2) Perform template matching on the original input image. (3) Detect

[8]https://www.docker.com/
[9]https://mqtt.org/
[10]https://opencv.org/

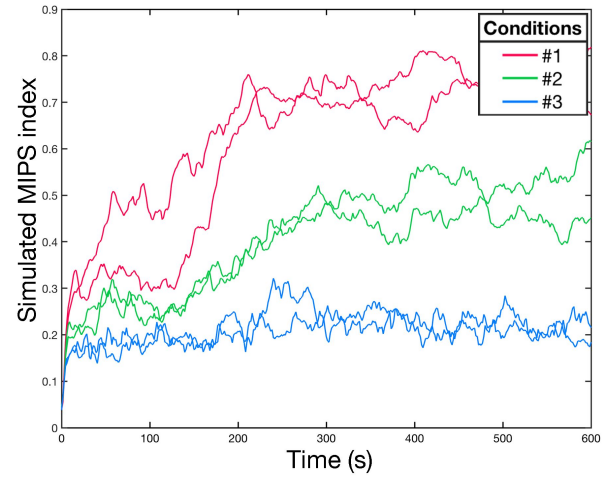

(a)

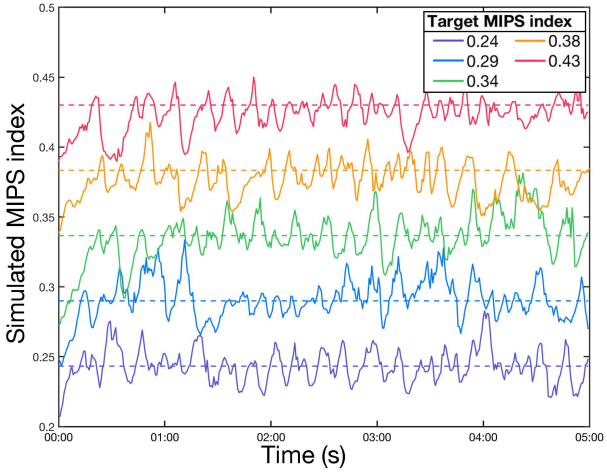

(b)

Fig. 10. (a) Open-loop simulation. Simulated MIPS trajectories under vibration conditions #1-3. The results of two simulations are reported for each condition. As also observed in Fig. 7(a) for the real micro bristle-robots, each condition leads to a distinct level of equilibrium MIPS index. (b) Closed-loop simulation. Simulation results of the closed-loop regulation of the MIPS index to different reference target values using vibration condition #1 and #3. This is analogous to what is shown in Fig. 9(b) for the case of the real micro bristle-robot swarm.

robots from template matching results and based on the threshold. Note that because of the high threshold, not all robots are detected. The detected ones are more likely to be the robots that are not inside clusters. (4) Use the detection as a mask and remove it from the original input. Use the modified image as the new input. Note that by removing these high confidence robots, robots that are originally inside clusters can be exposed. They would have higher confidence scores during the next template matching cycle. (5) Lower the threshold by a scaling factor ($\beta < 1$), such that the new threshold is $\alpha_0\beta$. (6) Repeat step 2-5 and merge the detection results until no more robots can be detected from template matching based on the updated threshold.

Robot direction detection uses principal component analysis (PCA) on the pixel coordinates of the red line indicator. The detailed procedure is as follows (Fig. 11): (1) From a still frame of the whole swarm, each individual robot is cropped

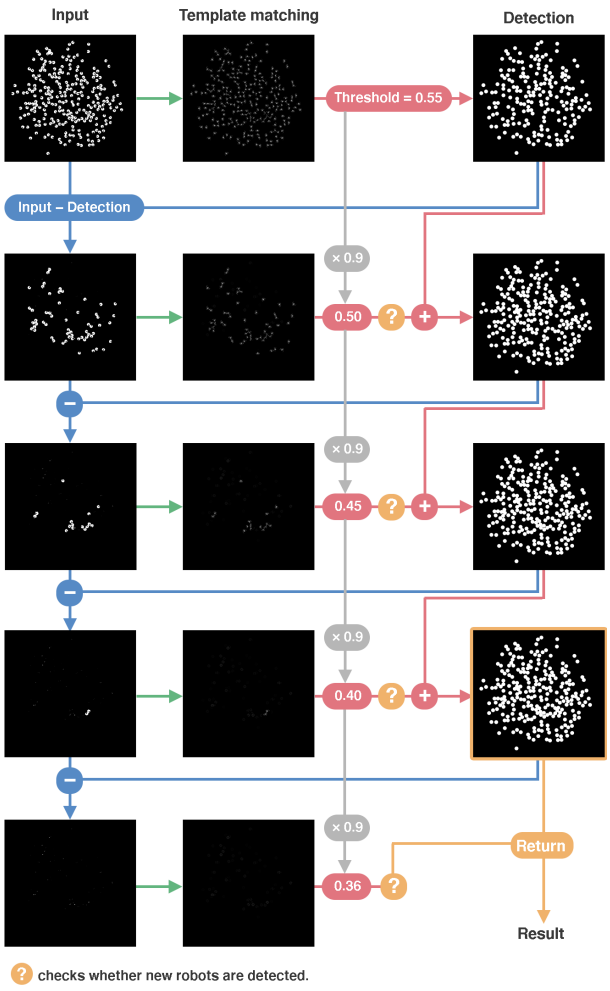

Fig. 11. Multi-stage template matching for robot tracking.

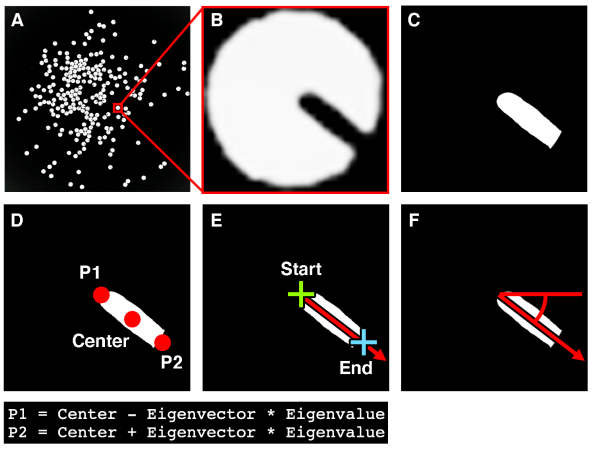

Fig. 12. Direction detection using principal component analysis (PCA).

out. (2) Through threshold and masking, a picture that only contains the orientation indicator is extracted. (3) Using PCA to get the eigenvectors and eigenvalues of the major axis and the center (mean) of the pixels. Two points P1 and P2 which fall on the major axis can be calculated based on these values. (4) Based on which point is closer to the center of the cropped image, P1 and P2 are determined to be either the start or the end point. (5) The locations of the start and end points are used to calculate the angle from the horizontal direction.

TABLE II
VIBRATION CONDITIONS AND ROBOT MOTILITY CHARACTERISTICS.

Condition number*	Amplitude (mm p-p)	Frequency (Hz)	Free speed (mm/s)	Rotational diffusion coefficient (rad^2/s)	Activity (rad^{-2})	Num of robots tested
1	0.0152	221.56	7.885	0.558	4.712	10
2	0.0152	239.32	8.042	0.608	4.410	10
3	0.0152	255.84	7.854	1.216	2.153	10
4	0.0152	271.36	8.406	0.962	2.914	10
5	0.0152	286.04	8.834	1.135	2.595	10
6	0.0152	300.00	9.168	0.574	5.327	10
7	0.0152	313.34	10.041	1.100	3.041	10
8	0.0152	326.13	10.317	1.248	2.755	10
9	0.0152	338.45	10.403	1.863	1.862	10
10	0.0152	350.32	10.471	1.542	2.264	10
11	0.0152	361.81	10.707	1.748	2.042	10
12	0.0110	300.00	6.616	0.121	18.253	5
13	0.0124	300.00	6.270	0.333	6.280	5
14	0.0138	300.00	7.777	0.422	6.142	5
15	0.0165	300.00	9.622	1.062	3.019	5
16	0.0179	300.00	10.753	1.795	1.996	5
17	0.0193	300.00	11.903	1.204	3.294	5
18	0.0207	300.00	13.316	0.965	4.601	5
19	0.0221	300.00	14.508	2.885	1.676	5
20	0.0096	300.00	4.464	0.162	9.169	3
21	0.0083	300.00	1.770	0.041	14.391	3
22	0.0234	300.00	16.044	5.931	0.902	3
23	0.0248	300.00	16.762	2.195	2.545	3
24	0.0152	372.95	10.594	0.967	3.652	3
25	0.0152	383.76	11.041	1.273	2.890	3
26	0.0124	271.36	7.317	0.356	6.849	3
27	0.0124	239.32	4.738	0.333	4.750	3
28	0.0124	326.13	7.553	0.669	3.764	3
29	0.0124	350.32	7.819	0.600	4.341	3
30	0.0124	372.95	8.393	0.495	5.654	3
31	0.0096	271.36	1.273	0.001	335.962†	3
32	0.0096	239.32	0.684	0.000	1477.783†	3
33	0.0096	326.13	5.643	0.440	4.274	3
34	0.0096	350.32	5.360	0.625	2.857	3
35	0.0096	372.95	5.779	1.385	1.391	3
36	0.0179	271.36	10.431	1.360	2.557	3
37	0.0179	239.32	9.252	0.995	3.099	3
38	0.0179	326.13	12.466	2.770	1.500	3
39	0.0179	350.32	12.143	2.919	1.387	3
40	0.0179	372.95	9.781	1.295	2.517	3
41	0.0207	271.36	13.022	1.222	3.554	3
42	0.0207	239.32	10.997	1.520	2.412	3
43	0.0207	326.13	14.528	2.673	1.811	3
44	0.0207	350.32	14.645	0.865	5.646	3
45	0.0207	372.95	15.379	1.757	2.917	3
46	0.0234	271.36	15.331	2.205	2.318	3
47	0.0234	239.32	13.282	4.850	0.913	3
48	0.0234	326.13	16.318	3.420	1.590	3
49	0.0234	350.32	16.285	6.177	0.879	3
50	0.0234	372.95	17.030	5.152	1.102	3

* The condition labels are different from vibration condition labels used in the main article.
† Large activity values in these cases are caused by computation errors when extracting small rotational diffusion coefficients.

APPENDIX D
TESTING CONDITIONS AND ROBOT CHARACTERISTICS

Including the 5 vibration conditions and results presented in the main text, 50 different vibration conditions were tested in total, as listed in Table II. Note that the condition labels are different from the labels used in the main text.

For each condition, robot free speed and rotational diffusion coefficient were extracted and presented in the table. The data was used to plot Fig. 4(a), 4(b), and 4(c).

REFERENCES

[1] J. Cortes, S. Martinez, T. Karatas, and F. Bullo, "Coverage control for mobile sensing networks," *IEEE Transactions on robotics and Automation*, vol. 20, no. 2, pp. 243–255, 2004.

[2] D. Albani, J. IJsselmuiden, R. Haken, and V. Trianni, "Monitoring and mapping with robot swarms for agricultural applications," in *2017 14th IEEE International Conference on Advanced Video and Signal Based Surveillance (AVSS)*. IEEE, 2017, pp. 1–6.

[3] J. Werfel, K. Petersen, and R. Nagpal, "Designing collective behavior in a termite-inspired robot construction team," *Science*, vol. 343, no. 6172, pp. 754–758, 2014.

[4] M. Senanayake, I. Senthooran, J. C. Barca, H. Chung, J. Kamruzzaman, and M. Murshed, "Search and tracking algorithms for swarms of robots: A survey," *Robotics and Autonomous Systems*, vol. 75, pp. 422–434, 2016.

[5] S. E. Chung, X. Dong, and M. Sitti, "Three-dimensional heterogeneous assembly of coded microgels using an untethered mobile microgripper," *Lab on a Chip*, vol. 15, no. 7, pp. 1667–1676, 2015.

[6] H. Wang *et al.*, "Automated assembly of vascular-like microtube with repetitive single-step contact manipulation," *IEEE Transactions on Biomedical Engineering*, vol. 62, no. 11, pp. 2620–2628, 2015.

[7] M. Brambilla, E. Ferrante, M. Birattari, and M. Dorigo, "Swarm robotics: a review from the swarm engineering perspective," *Swarm Intelligence*, vol. 7, no. 1, pp. 1–41, 2013.

[8] E. Şahin, "Swarm robotics: From sources of inspiration to domains of application," in *Swarm Robotics*, E. Şahin and W. M. Spears, Eds. Springer Berlin Heidelberg, 2005, pp. 10–20.

[9] O. Soysal and E. Sahin, "Probabilistic aggregation strategies in swarm robotic systems," in *Proceedings 2005 IEEE Swarm Intelligence Symposium, 2005. SIS 2005.* IEEE, 2005, pp. 325–332.

[10] F. Qiu, S. Fujita, R. Mhanna, L. Zhang, B. R. Simona, and B. J. Nelson, "Magnetic helical microswimmers functionalized with lipoplexes for targeted gene delivery," *Advanced Functional Materials*, vol. 25, no. 11, pp. 1666–1671, 2015.

[11] R. Mhanna *et al.*, "Artificial bacterial flagella for remote-controlled targeted single-cell drug delivery," *Small*, vol. 10, no. 10, pp. 1953–1957, 2014.

[12] E. B. Steager, M. Selman Sakar, C. Magee, M. Kennedy, A. Cowley, and V. Kumar, "Automated biomanipulation of single cells using magnetic microrobots," *The International Journal of Robotics Research*, vol. 32, no. 3, pp. 346–359, 2013.

[13] X. Yan *et al.*, "Multifunctional biohybrid magnetite microrobots for imaging-guided therapy," *Science Robotics*, vol. 2, no. 12, 2017.

[14] H. Xie *et al.*, "Reconfigurable magnetic microrobot swarm: Multimode transformation, locomotion, and manipulation," *Science Robotics*, vol. 4, no. 28, 2019.

[15] I. D. Couzin, "Collective cognition in animal groups," *Trends in cognitive sciences*, vol. 13, no. 1, pp. 36–43, 2009.

[16] G. Gompper *et al.*, "The 2020 motile active matter roadmap," *Journal of Physics: Condensed Matter*, vol. 32, no. 19, p. 193001, 2020.

[17] J. Aguilar *et al.*, "Collective clog control: Optimizing traffic flow in confined biological and robophysical excavation," *Science*, vol. 361, no. 6403, pp. 672–677, 2018.

[18] D. M. Gordon, "Behavioral flexibility and the foraging ecology of seed-eating ants," *The American Naturalist*, vol. 138, no. 2, pp. 379–411, 1991.

[19] U. Lopez, J. Gautrais, I. D. Couzin, and G. Theraulaz, "From behavioural analyses to models of collective motion in fish schools," *Interface focus*, vol. 2, no. 6, pp. 693–707, 2012.

[20] J.-L. Deneubourg, J.-C. Grégoire, and E. Le Fort, "Kinetics of larval gregarious behavior in the bark beetledendroctonus micans (coleoptera: Scolytidae)," *Journal of Insect Behavior*, vol. 3, no. 2, pp. 169–182, 1990.

[21] W. C. Allee, "Animal aggregations," *The Quarterly Review of Biology*, vol. 2, no. 3, pp. 367–398, 1927.

[22] M. B. Miller and B. L. Bassler, "Quorum sensing in bacteria," *Annual Reviews in Microbiology*, vol. 55, no. 1, pp. 165–199, 2001.

[23] L. Hall-Stoodley, J. W. Costerton, and P. Stoodley, "Bacterial biofilms: from the natural environment to infectious diseases," *Nature reviews microbiology*, vol. 2, no. 2, pp. 95–108, 2004.

[24] J. Stenhammar, A. Tiribocchi, R. J. Allen, D. Marenduzzo, and M. E. Cates, "Continuum theory of phase separation kinetics for active brownian particles," *Phys. Rev. Lett.*, vol. 111, p. 145702, Oct 2013.

[25] I. Theurkauff, C. Cottin-Bizonne, J. Palacci, C. Ybert, and L. Bocquet, "Dynamic clustering in active colloidal suspensions with chemical signaling," *Physical review letters*, vol. 108, no. 26, p. 268303, 2012.

[26] M. E. Cates and J. Tailleur, "Motility-induced phase separation," *Annu. Rev. Condens. Matter Phys.*, vol. 6, no. 1, pp. 219–244, 2015.

[27] A. P. Solon, J. Stenhammar, M. E. Cates, Y. Kafri, and J. Tailleur, "Generalized thermodynamics of motility-induced phase separation: phase equilibria, laplace pressure, and change of ensembles," *New Journal of Physics*, vol. 20, no. 7, p. 075001, 2018.

[28] M. W. Zemansky *et al.*, "Heat and thermodynamics," 1943.

[29] S. Mayya, G. Notomista, D. Shell, S. Hutchinson, and M. Egerstedt, "Non-uniform robot densities in vibration driven swarms using phase separation theory," in *2019 IEEE/RSJ International Conference on Intelligent Robots and Systems (IROS)*. IEEE, 2019, pp. 4106–4112.

[30] D. Jang, J. Jeong, H. Song, and S. K. Chung, "Targeted drug delivery technology using untethered microrobots: A review," *Journal of Micromechanics and Microengineering*, vol. 29, no. 5, p. 053002, 2019.

[31] K. Ioi, "A mobile micro-robot using centrifugal forces," in *1999 IEEE/ASME International Conference on Advanced Intelligent Mechatronics (Cat. No.99TH8399)*, 1999, pp. 736–741.

[32] D. Kim, Z. Hao, J. Ueda, and A. Ansari, "A 5 mg micro-bristle-bot fabricated by two-photon lithography," *Journal of Micromechanics and Microengineering*, vol. 29, no. 10, p. 105006, aug 2019.

[33] D. Kim, Z. Hao, A. Mohazab, and A. Ansari, "On the forward and backward motion of milli-bristlebots," *International Journal of Non-Linear Mechanics*, vol. 127, p. 103551, 2020.

[34] Z. Hao, D. Kim, A. R. Mohazab, and A. Ansari, "Maneuver at micro scale: Steering by actuation frequency control in micro bristle robots*," in *2020 IEEE International Conference on Robotics and Automation (ICRA)*, 2020, pp. 10 299–10 304.

[35] F. Becker, S. Boerner, V. Lysenko, I. Zeidis, and K. Zimmermann, "On the mechanics of bristle-bots - modeling, simulation and experiments," in *ISR/Robotik 2014; 41st International Symposium on Robotics*, 2014, pp. 1–6.

[36] F. Becker, "An approach to the dynamics of vibration-driven robots with bristles," *IFAC-PapersOnLine*, vol. 48, no. 1, pp. 842–843, 2015, 8th Vienna International Conferenceon Mathematical Modelling.

[37] G. Notomista, S. Mayya, A. Mazumdar, S. Hutchinson, and M. Egerstedt, "A study of a class of vibration-driven robots: Modeling, analysis, control and design of the brushbot," in *2019 IEEE/RSJ International Conference on Intelligent Robots and Systems (IROS)*. IEEE, 2019, pp. 5101–5106.

[38] S. Thutupalli, D. Geyer, R. Singh, R. Adhikari, and H. A. Stone, "Flow-induced phase separation of active particles is controlled by boundary conditions," *Proceedings of the National Academy of Sciences*, vol. 115, no. 21, pp. 5403–5408, 2018.

[39] B. Lindner and E. Nicola, "Diffusion in different models of active brownian motion," *The European Physical Journal Special Topics*, vol. 157, no. 1, pp. 43–52, 2008.

[40] J. H. Conway and N. J. A. Sloane, *Sphere packings, lattices and groups*. Springer Science & Business Media, 2013, vol. 290.

[41] Y. Fily, S. Henkes, and M. C. Marchetti, "Freezing and phase separation of self-propelled disks," *Soft matter*, vol. 10, no. 13, pp. 2132–2140, 2014.

[42] S. Miller and D. Childers, *Probability and random processes: With applications to signal processing and communications*. Academic Press, 2012.

[43] Á. Mulero, *Theory and simulation of hard-sphere fluids and related systems*. Springer, 2008, vol. 753.

[44] S. Mayya, P. Pierpaoli, G. Nair, and M. Egerstedt, "Localization in densely packed swarms using interrobot collisions as a sensing modality," *IEEE Transactions on Robotics*, vol. 35, no. 1, pp. 21–34, 2018.

[45] W.-H. Liu and A. H. Sherman, "Comparative analysis of the cuthill–mckee and the reverse cuthill–mckee ordering algorithms for sparse matrices," *SIAM Journal on Numerical Analysis*, vol. 13, no. 2, pp. 198–213, 1976.

[46] E. Schubert, J. Sander, M. Ester, H. P. Kriegel, and X. Xu, "Dbscan revisited, revisited: why and how you should (still) use dbscan," *ACM Transactions on Database Systems (TODS)*, vol. 42, no. 3, pp. 1–21, 2017.

[47] J. Matousek, *Geometric discrepancy: An illustrated guide*. Springer Science & Business Media, 2009, vol. 18.

[48] J. H. Myers, "Selecting a measure of dispersion," *Environmental Entomology*, vol. 7, no. 5, pp. 619–621, 1978.

[49] S. M. LaValle, *Planning algorithms*. Cambridge university press, 2006.

Zhijian Hao (Student Member, IEEE) received the B.S.E. degree in electrical engineering from University of Michigan, Ann Arbor, MI, USA, in 2018, the M.S. degree in electrical and computer engineering from Georgia Institute of Technology, Atlanta, GA, USA, in 2020.

He is currently working toward the Ph.D. degree in electrical and computer engineering, focusing on swarm robotics and sensor technology, in Georgia Institute of Technology, Atlanta, GA, USA.

Siddharth Mayya (Member, IEEE) received the B.Tech. degree in electronics and communication engineering from the Manipal Institute of Technology, Manipal, India, in 2014, and the M.S. and Ph.D. degree in electrical and computer engineering from the Georgia Institute of Technology, Atlanta, GA, USA, in 2016 and 2019, respectively.

Prior to joining Amazon Robotics in 2021, he was a Postdoctoral Researcher in the GRASP Lab at the University of Pennsylvania. He is currently an applied scientist at Amazon Robotics, located in North Reading, MA, USA.

Dr. Mayya is the lead guest editor for a special issue in the Springer Autonomous Robots journal (2021-2022). He is a recipient of the best paper award at the IEEE Conference on Advanced Robotics and its Social Impacts 2022 and a finalist for the outstanding paper award at the IEEE International Symposium on Multi-Robot and Multi-agent Systems 2019.

Gennaro Notomista (Member, IEEE) received a B.S. degree in mechanical engineering from the Università degli Studi di Napoli "Federico II", Napoli, Italy, in 2012, a M.Eng. degree in automotive engineering from the Technische Hochschule Ingolstadt, Ingolstadt, Germany, in 2015, a M.S. degree in mechanical engineering from the Università degli Studi di Napoli "Federico II", Napoli, Italy, in 2016, a M.S. degree in mathematics and a Ph.D. degree in robotics from the Georgia Institute of Technology, Atlanta, GA, USA in 2019 and 2020, respectively.

He is currently an Assistant Professor in the Department of Electrical and Computer Engineering at the University of Waterloo, Waterloo, ON, Canada. Prior to joining University of Waterloo, he was a post-doctoral researcher at the CNRS/Inria/IRISA, Rennes, France. His main research interests lie at the intersection of design and control of robotic systems for long-duration autonomy with applications to environmental monitoring.

Dr. Notomista is a Fulbright Scholar and was the recipient of the Alumni Small Grant (2020) and the IEEE ARSO Best Paper Award (2022). He is an associate editor of the IEEE Robotics and Automation Letters.

Seth Hutchinson (Fellow, IEEE) is Professor and KUKA Chair for Robotics in the School of Interactive Computing at the Georgia Institute of Technology. He received his Ph.D. from Purdue University in 1988, then joined the University of Illinois, where he was a Professor of Electrical and Computer Engineering until 2017. Hutchinson served as Editor-in-Chief for the "IEEE Trans. on Robotics" and was founding Editor-in-Chief of the RAS Conference Editorial Board. He has more than 300 publications on the topics of robotics and computer vision, and is coauthor of two books on robotics. He is a Fellow of the IEEE.

Magnus Egerstedt (Fellow, IEEE) is the Dean of Engineering and a Professor in the Department of Electrical Engineering and Computer Science at the University of California, Irvine. He received the M.S. degree in Engineering Physics and the Ph.D. degree in Applied Mathematics from the Royal Institute of Technology, Stockholm, Sweden, the B.A. degree in Philosophy from Stockholm University. Dr. Egerstedt conducts research in the areas of control theory and robotics, with particular focus on control and coordination of multi-robot systems. He is a Fellow of IEEE and IFAC and a member of the Royal Swedish Academy of Engineering Science.

Azadeh Ansari (Member, IEEE) received the B.S. degree in electrical engineering from the Sharif University of Technology, Tehran, Iran, in 2010, and the M.S. and Ph.D. degrees in electrical engineering from the University of Michigan, Ann Arbor, in 2013 and 2016, respectively. She is currently the Sutterfield family Assistant Professor with the School of Electrical and Computer Engineering, Georgia Institute of Technology. Prior to joining the ECE Faculty, she was a Post-Doctoral Scholar with the Department of Physics, California Institute of Technology. Her research interests cover nano/micro electromechanical systems (N/MEMS) and microscale robotics. She is the recipient of the 2021 Roger Webb Outstanding Junior Faculty Award at Georgia Tech, the 2020 NSF CAREER Award and the 2017 ProQuest Distinguished Dissertation Award from the University of Michigan.